

In-Situ Construction of La-B Co-Doped g-C₃N₄ for Highly Efficient Photocatalytic H₂ Production and RhB Degradation

L. N. Wang¹, L. H. Xiao², Q. Jin², and Q. Chang^{1*}

¹ Key Laboratory of Resources Conversion and Pollution Control of the State Ethnic Affairs Commission, College of Resources and Environmental Science, South-Central Minzu University, Wuhan 430074, China

² Shandong Key Laboratory of Water Pollution Control and Resource Reuse, School of Environmental Science and Engineering, Shandong University, Qingdao 266237, China

Received 16 January 2022; revised 03 March 2022; accepted 04 May 2022; published online 27 June 2022

ABSTRACT. Doped graphitic carbon nitride (g-C₃N₄) has been investigated as the visible light photocatalyst for photocatalytic H₂ production and organic pollution removal. The elements doping could change the nanostructures, surface composition, and electronic structures compared to pure g-C₃N₄. Such changes will provide better light-harvesting, more active sites and enhanced charge separation. In this work, we built the La-B co-doped g-C₃N₄ by an in-situ growth of g-C₃N₄ on LaB₆. The effect of La-B co-doping on the phase, morphology, light absorption and porous structures is fully characterized to clearly understand the differences in the photocatalytic activities clearly. La and B co-doping introduced defect states and redistribution with suitable redox potentials, benefiting charge separation and photocatalytic reactions. So, the optimal co-doped samples process a higher photocatalytic performance in H₂ production and Rhodamine B (RhB) degradation than the pure g-C₃N₄. The possible valence and conduction band edge positions and photocatalytic mechanism are discussed at last.

Keywords: g-C₃N₄, photocatalysts, B-doped, La-doped, H₂ production

1. Introduction

The growing demand for renewable fossil fuels and environmental applications of functional materials has become one of the most urgent issues in our fast-growing and long-term sustainable developing society (Chang and Kashani, 2009; Miao et al., 2014; Dhanushkodi et al., 2015; Xiao et al., 2015; Lin et al., 2018; Liu et al., 2016; Liu et al., 2018). So, considerable researchers have been prompted to use different methods to solve the severe environmental and energy crisis (Miao et al., 2014; Yu et al., 2017; Ren et al., 2020; Zhang et al., 2020; Anaraki et al., 2022; Dai et al., 2022). In particular, semiconductor photocatalysis using clean solar energy can degrade various pollutants (such as organic pollutants, heavy metals and volatile organic compounds) or produce organic fuels from water or green house gaseous CO₂, which have been considered eco-friendly technology for water & air purification and energy fuel production (Li et al., 2021a; Xiao et al., 2021; Qu et al., 2022; Zhang et al., 2022). Many studies on nanostructured photocatalysts have been carried out to improve photocatalytic performances in pollutants removal and fuels production (He et al., 2018, 2020; Muhammad et al., 2020; Li et al., 2021b; Zhang et al., 2021; Yu et al., 2022). Graphitic carbon nitride (g-C₃N₄) has

been one of the common visible-light-driven photocatalysts in recent years. Many related papers have been published every year (Yuan et al., 2015; Mavengere and Kim, 2020; Tang et al., 2020; Yu et al., 2021; Zhao et al., 2021). The tunable electron configuration and good chemical and thermal stability make it a promising candidate for practical photocatalytic applications. The pure g-C₃N₄ also has been limited by many disadvantages, such as fast recombination of photogenerated charges, inefficient usage of visible light (a relatively larger bandgap around 2.72 eV), and small surface area, which results in a low visible-light-driven photocatalytic activity for hydrogen production and removal of organic pollutants (Ong et al., 2016; Ngullie et al., 2020; Cheng et al., 2021; Shen et al., 2021). The regulation design of the g-C₃N₄ photocatalyst's electronic structure plays a vital function in improving the photocatalytic efficiency (Fu et al., 2018; Zhang et al., 2021). A series of metal or nonmetal dopants have been considered to improve the photocatalytic activities (Lan et al., 2017; Ou et al., 2017). The doping could change the nanostructure (which will affect the absorption of photons or reactants) and electronic structures (such as band position and defect energy level, which will affect the charge transmission and separation) of doped g-C₃N₄, which provide better light-harvesting, more active center and enhanced charge separation. The interactions between precursor molecules and doping elements in the doping strategy are significant for these changes, which results in different photocatalytic performances (Jiang et al., 2018). The metallic dopants formed chemical bonding with O or N into tri-s-triazine units in the g-C₃N₄ network,

* Corresponding author. Tel.: +862767843918.

E-mail address: changqinghust@163.com (Q. Chang).

while nonmetal dopants often interacted with the N or O in the g-C₃N₄ network. Therefore, charge depletion occurred on the dopants' positions and then migrated from dopants to the surrounding carbon or nitrogen atoms of g-C₃N₄, which indicated the stable chemical interactions between various doped components and g-C₃N₄.

Recently, many researchers have synthesized the B-doped g-C₃N₄ for enhancing the photocatalytic performance, and such enhanced performance originates from the smaller bandgap, more active sites and the better conductivity resulting from B-doping (Yan et al., 2010; Thaweesak et al., 2017; Wang et al., 2018a; Wang et al., 2018b; Yan et al., 2018). The superior photocatalytic performances are related to the mesopores formation, more defect sites, and smaller bandgap after B doping, resulting in abundant reactive sites on the photocatalyst and improving the efficiencies of charge transfer and separation (Yao et al., 2020). Yan et al. (2010) prepared B doped g-C₃N₄ using boron oxide and melamine via a heating process in 2010 and the products showed enhanced photocatalytic degradation performances investigated against Rhodamine B (RhB) and Methyl Orange (MO), which was attributed to the extended light absorption and the defected structure induced by boron doping. Thaweesak et al. (2017) synthesized B-doped g-C₃N₄ nano-sheets via a facile one-pot polycondensation process. The decreased bandgap by B-doping can effectively reduce the photo-excited charge recombination and increase light-harvesting resulting in the best photocatalytic performance for H₂ evolution. Compared to B-doping, La atoms possess larger atom radius, lower electronegativity, and weak interaction between the lone pair of nucleus and electrons. Only a few researchers have focused their eyes on La modified g-C₃N₄ to enhance photocatalytic performance (Rong et al., 2015; Bouzidi et al., 2020; Muhammad et al., 2020). For example, La³⁺ donor doping can effectively improve the photocatalytic efficiency of g-C₃N₄, resulting from enhanced optical absorption, reduced particle size, as well as efficient charge separation (Bouzidi et al., 2020; Muhammad et al., 2020; Li et al., 2021c; Tasleem and Tahir, 2021). In addition, g-C₃N₄ doped with different amounts of La₂O₃ are also synthesized by a facile ultrasound-assisted calcination process and show improved photocatalytic degradation rate for tetracycline hydrochloride, which is related to the low recombination of electrons and holes between interfaces in such system (Zhu et al., 2021).

Recently, metal and nonmetal co-doping has been proved to be an efficient strategy to improve the photocatalytic performances, which can result in a decreased bandgap, formation of mesopore and a lower recombination of photogenerated charge (Cao et al., 2010; Zhang et al., 2014; Youssef and Yakout, 2020). Metal and B co-doping g-C₃N₄ have been reported to improve photocatalytic performances. Bhagat and Dashora (2021) highlighted the synergistic effect of Co-B co-doping g-C₃N₄ in terms of formation of impurity state, high light absorption, charge redistribution and electronic structures with suitable redox potentials compared to pure g-C₃N₄, which suggests Co-B co-doped g-C₃N₄ as a potential candidate for visible-light-driven photocatalytic water splitting. Yao et al. (2020) reported that Ag-B doped g-C₃N₄ was prepared by an in-situ decomposition ther-

mal polymerization method with enhanced photocatalytic nitrogen fixation. The Ag/B-doped g-C₃N₄ exhibited reduced band gap and accelerated charge separation. Wang et al. (2021a) found that K-B co-doped g-C₃N₄ exhibited the highest photocatalytic vapor water splitting performance compared with the K doped and pristine g-C₃N₄ samples, which could be attributed to the improved separation of photoinduced carriers resulting from B and K co-doping. Guo et al. (2021) prepared a direct Z-scheme heterojunction constructed between MoS₂ and Eu-B co-doped g-C₃N₄ with enhanced photodegradation of tetracycline, which efficiently extended the visible-light absorption range and promoted the photogenerated carrier separation. The Cr-B co-doping could reduce the bandgap and introduce impurity levels by the synergistic effect of Cr-3d and B-2p states, which was confirmed in the Cr-B co-doped g-C₃N₄/BiVO₄ system by using Heyd-Scuseria-Ernzerhof (HSE06) hybrid functional method calculations (Wang et al., 2021b). Besides, Chen et al. (2019) addressed that a new strategy of O/La co-functionalized amorphous carbon nitride showed highly boosted photocatalytic performance for NO removal, which was attributed to the formation of electronic channels for directional electron delivery and the generation of localized electrons for enhanced reactants activation.

La-B co-doped TiO₂ and BiVO₄ have been proved to process enhanced photocatalytic degradation performances due to the synergistic effect of the La-B co-doped ions (Liu et al., 2011; Wang et al., 2013). The results showed that La and B ions were incorporated into the lattice, resulting in a narrow bandgap and high light absorbance in the visible region. Furthermore, La-B co-doping could lead to more surface oxygen vacancies and high specific surface areas, which could help the separation of photogenerated electrons (Wang et al., 2013). Herein, we prepared the La-B co-doped g-C₃N₄ photocatalysts and investigated their visible-light-driven photocatalytic performance in H₂ production and degradation of RhB. The synergistic effect of La-B co-doped on the phase, morphology, light absorption, and porous structures is fully characterized to clearly understand the differences in the photocatalytic activities. Moreover, the possible band position was discussed at last.

2. Materials and Methods

2.1. Preparation of La-B Co-Doped g-C₃N₄ Composites

The synthesis process of La-B co-doped g-C₃N₄ composites was described as follows: First, a 0.5 g dicyandiamide (C₂H₄N₄ ≥ 99.0%) powders with different amounts of lanthanum boride (LaB₆ ≥ 99.0%) were fully mixed and vigorously ground for several minutes. Second, the mixed powders were transferred into a 35 mL crucible with a cover and calcinated at 500 °C for 2 h in a muffle furnace. Then, the obtained powders were washed with deionized water and ethanol several times. Finally, the La-B co-doped g-C₃N₄ products were obtained after drying in the oven overnight. Different amounts of LaB₆ (0, 0.025, 0.050, 0.075, and 0.100 g) were integrated in the g-C₃N₄. According to the amount of LaB₆ added, the obtained products were marked as g-C₃N₄, 0.025-LBCN, 0.050-LBCN, 0.075-LBCN, and 0.100-LBCN, respectively.

2.2. Characterization

The morphology and nanostructure of the co-doped $g\text{-C}_3\text{N}_4$ samples were investigated via a scanning electron microscope (SEM, FEI Quanta FEG 250, USA) and a high-resolution transmission electron microscope (HR-TEM, JEOL JEM-2100 Plus, Japan). The X-ray diffraction spectroscopy (XRD, Rigaku Ultima IV, Japan) was used to identify the phase of as-prepared co-doped $g\text{-C}_3\text{N}_4$ samples. Also, the photo-absorption capability was determined by a UV-Vis spectrophotometer (Shimadzu UV-2600, Japan). The nitrogen adsorption-desorption isotherm was analyzed using a nitrogen adsorption apparatus (JW-BK 200B, China), and the specific surface areas and pore size distribution plots were also analyzed with the same machine. Finally, the surface composition, elemental chemical state, and valence band (VB) positions of the co-doped samples were employed on an X-ray photoelectron spectrometer (XPS, Thermo Scientific K-Alpha, US).

2.3. Photocatalytic Measurements

2.3.1. H_2 Production

For the photocatalytic H_2 production activity tests: 20 mg as-prepared catalyst was dispersed in 40 mL aqueous solution with 10 vol.% of methanol (4 mL methanol and 36 mL deionized water). After ultrasonic dispersion for 2 mins, the pH of the obtained suspension was slowly adjusted to 3.0 under continuously stirring. Subsequently, the obtained suspension was transferred into a Pyrex reactor and covered by a rubber septum. Argon gas was aerated after vacuum to remove dissolved oxygen before the photocatalytic reaction. A 300 W Xe-arc lamp with a visible filter ($\lambda > 420$ nm) was used as the light source in our photocatalytic measurements. The produced H_2 in the top space of the sealed reactor was analyzed online by a gas chromatograph (GC, Fuli GC-9790II) with a thermal conductivity detector and argon gas as the carrier gas. The photocatalytic stability in hydrogen production activity was determined by repeating four cycles in the same sealed Pyrex reactor. The gaseous products were removed at the end of each cycle and the argon gas was pumped at the beginning of the next cycle.

2.3.2. Degradation of RhB

In photocatalytic degradation measurement: 20 mg of the photocatalyst was added into a Pyrex reactor with 100 mL of 10 ppm RhB. Then, a 300 W Xe-arc lamp with a VisREF filter (350 ~ 780 nm) was used for the photoreaction after 30 mins of adsorption equilibrium in the dark. The reactor was stirred magnetically all through the photocatalytic degradation process. 1.5 mL of the suspensions were withdrawn from the reactor intermittently at certain time intervals and filtered through a 45 μm PTFE syringe filter. An UV-Vis spectrophotometer (Shimadzu UV-2600, Japan) was used to determine the concentration of RhB, and the absorption values calculated the degradation percentage at 554 nm (Feng et al., 2018).

3. Results and Discussion

3.1. Characterization of Photocatalysts

A series of La-B co-doped $g\text{-C}_3\text{N}_4$ were successfully syn-

thesized by calcination to 500 $^\circ\text{C}$ in the air for 2 h, where the lanthanum boride ($\text{LaB}_6 \geq 99.0\%$) and dicyandiamide ($\text{C}_2\text{H}_4\text{N}_4 \geq 99.0\%$) powders were used as raw materials. As mentioned in the introduction part, the doping could change nanostructure (which will affect the absorption of photons or reactants) and electronic structures (such as band position and defect energy level, which will affect the charge transmission and separation). The interactions between the doping atoms and precursor molecules in the preparation strategy are essential to the doped $g\text{-C}_3\text{N}_4$ samples, leading to various electronic structures and physicochemical properties and thus affecting the photocatalytic performances. Therefore, the phase, morphology, light absorption and porous structures are fully characterized by using various technologies.

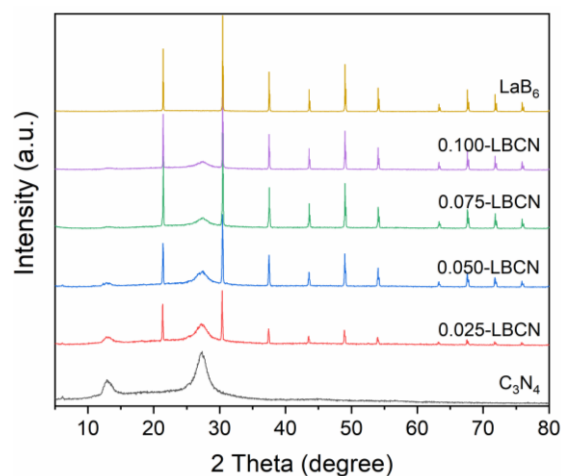


Figure 1. XRD patterns of the as-obtained samples.

3.1.1. Crystal Structure of the Photocatalysts

Figure 1 presents the X-ray diffraction patterns of pure $g\text{-C}_3\text{N}_4$ and La-B co-doped $g\text{-C}_3\text{N}_4$. The two distinct diffraction peaks at scattering angles of 13.1° and 27.8° correspond to the (100) and (002) diffraction planes of $g\text{-C}_3\text{N}_4$ (JCPDS 87-1562), which indicate the characteristic interlayer stacking structure of graphite C_3N_4 (Feng et al., 2018). For the La-B co-doped samples, the peaks at scattering angles of 21.35° , 30.38° , 37.44° , and 48.97° correspond to (100), (110), (111), and (210) crystal planes of LaB_6 , respectively. All peaks can be readily indexed as the cubic phase of LaB_6 (JCPDS card No.34-0427) with lattice constants $a = 4.1569 \text{ \AA}$, $b = 4.1569 \text{ \AA}$, $c = 4.1569 \text{ \AA}$. The intensity of LaB_6 diffraction peaks increased with LaB_6 addition during the preparation process, which indicates the LaB_6 was not fully doped into the $g\text{-C}_3\text{N}_4$ lattice. La atoms will form chemical bonding with the tri-s-triazine units in $g\text{-C}_3\text{N}_4$, while the B atoms interact with the C, N, or O in the $g\text{-C}_3\text{N}_4$ network, which will be discussed in the XPS part. It also should be noted here that the diffraction peaks from $g\text{-C}_3\text{N}_4$ could be found in all co-doped samples.

3.1.2. Morphologies of the Photocatalysts

The morphologies and nanostructures of as-obtained prod-

ucts are checked by using SEM and TEM, and the corresponding images are shown in Figure 2 and 3, respectively. As shown in Figure 2, it could be seen that the LaB₆ addition had effects on the morphology. The pure g-C₃N₄ illustrated a typical irregular bulk structure with a smooth surface. The surface became coarse after interaction with LaB₆. The nanorod and nanofiber-like structures were appeared on the surface of catalysts in the 0.050-LBCN and 0.075-LBCN. By the way, the pure LaB₆ after 500 °C treated showed small nanoparticles without nanorods or

nanofibers coverage on the surface, which also indicated that LaB₆ reacted with dicyandiamide and affected the morphologies of the products. The structure of 0.075-LBCN was further checked by the HR-TEM, the clear layered structure of g-C₃N₄ could be seen in Figure 3a ~ c, and the element mapping data were used to investigate the elements' distribution. La, B, C and N show a uniform distribution throughout the whole selected area, as shown in Figure 3d, indicating that La-B was co-doped into the samples.

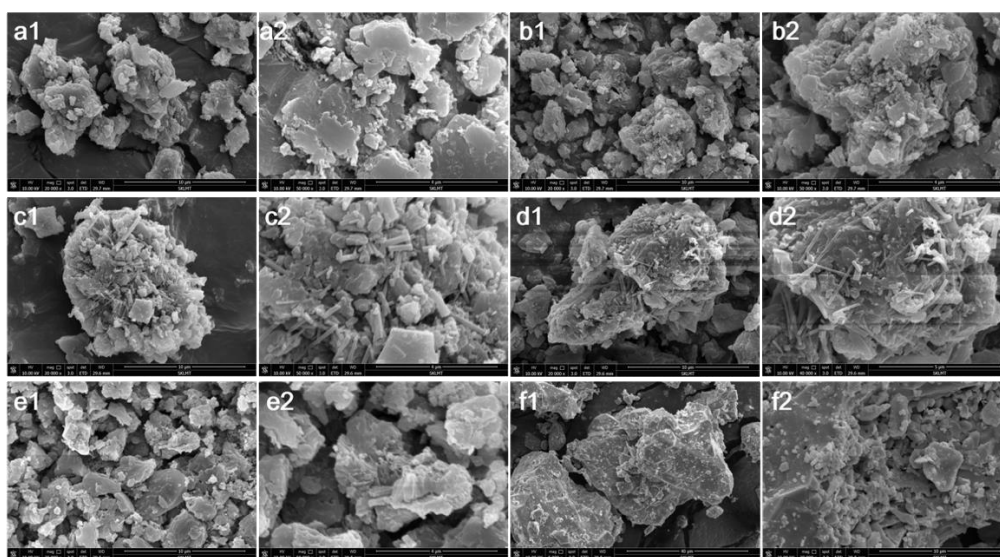


Figure 2. SEM images of the as-obtained samples under different magnifications: (a) g-C₃N₄; (b) 0.025-LBCN; (c) 0.050-LBCN; (d) 0.075-LBCN; (e) 0.100-LBCN; (f) LaB₆-500 °C.

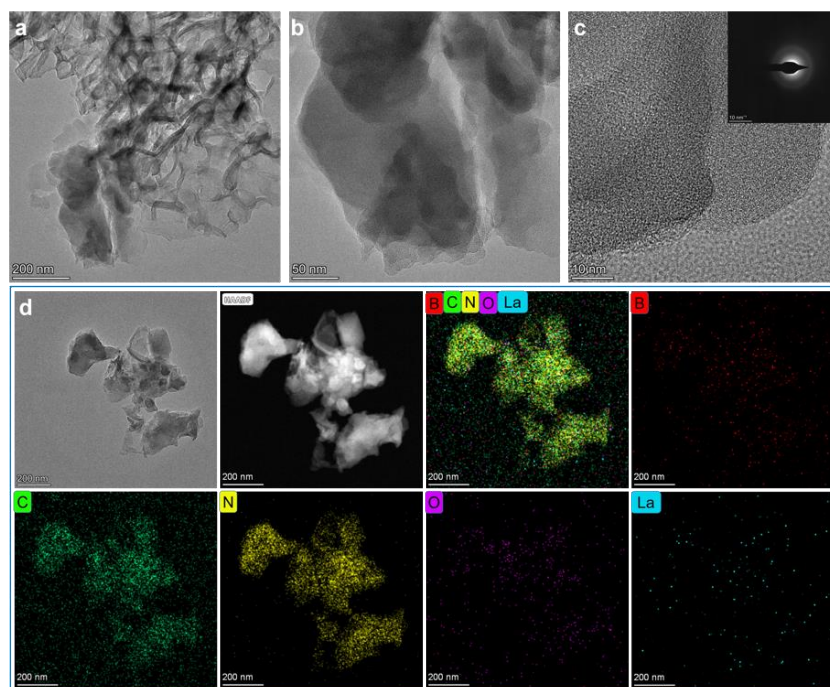


Figure 3. (a ~ c) TEM images of the 0.075-LBCN sample; (d) the elements mapping data of B, C, N, O, and La elements in the 0.075-LBCN sample.

3.1.3. Optical and Porosity Properties of the Photocatalysts

The light absorption spectra of the pure and co-doped $g\text{-C}_3\text{N}_4$ samples were determined on a UV-vis spectrophotometer. As shown in Figure 4a, LaB_6 calcined at $500\text{ }^\circ\text{C}$ in the air for 2h exhibits strong absorption in the full spectrum. The absorption spectra showed an increased absorption in the visible region compared with pure $g\text{-C}_3\text{N}_4$, which was related to the La-B co-doping in the hybrid samples. The La-B co-doped samples did not significantly enhance absorption performance in the visible region due to the $g\text{-C}_3\text{N}_4$'s coverage. The bandgaps were estimated by the Tauc plot, as shown in Figure 4b (He et al., 2017). The values of bandgaps show a little change and the detailed data is listed in Table 1, and such little change also indicates that just some La-B atoms interact with the $g\text{-C}_3\text{N}_4$ network.

The addition of LaB_6 also affects the surface area and pore size distribution of the catalysts, so porosity properties were analyzed using a nitrogen adsorption apparatus. The nitrogen adsorption-desorption plots of the various samples are presented in Figure 4c. The H3 type N_2 adsorption isotherm with a hysteresis loop were observed. Such pores include flat plate slit structure and crack and wedge structure, given by the flaky nanoparticles. The Brunauer-Emmett-Teller (BET) surface area of the $g\text{-C}_3\text{N}_4$ and co-doped $g\text{-C}_3\text{N}_4$ are listed in Table 1. 6.331, 6.266, 7.811, 7.290, and $6.910\text{ m}^2/\text{g}$ for $g\text{-C}_3\text{N}_4$, 0.025-LBCN, 0.050-LBCN, 0.075-LBCN, and 0.100-LBCN, respectively. The surface area slightly increases after LaB_6 addition compared with the pure $g\text{-C}_3\text{N}_4$. Besides, there are few differences in the corresponding Barrett-Joyner-Halenda (BJH) pore size distribution between pure $g\text{-C}_3\text{N}_4$ and x-LBCN samples (Figure 4d).

Table 1. The Surface Area, Bandgap and Photocatalytic Activities of the x-LBCN Samples

Samples	Surface Area (m^2/g)	Bandgap (eV)	H_2 production ($\mu\text{mol}/\text{g}/\text{h}$)	RhB Removal in 2 h (%)	Degradation Rate Constant (k) Values
C_3N_4	6.331	2.68	895	74.48	0.01096
0.025-LBCN	6.266	2.71	1298	95.11	0.02315
0.050-LBCN	7.811	2.77	1543	89.13	0.01765
0.075-LBCN	7.290	2.71	1693	77.17	0.01256
0.100-LBCN	6.910	2.73	1270	77.87	0.01210

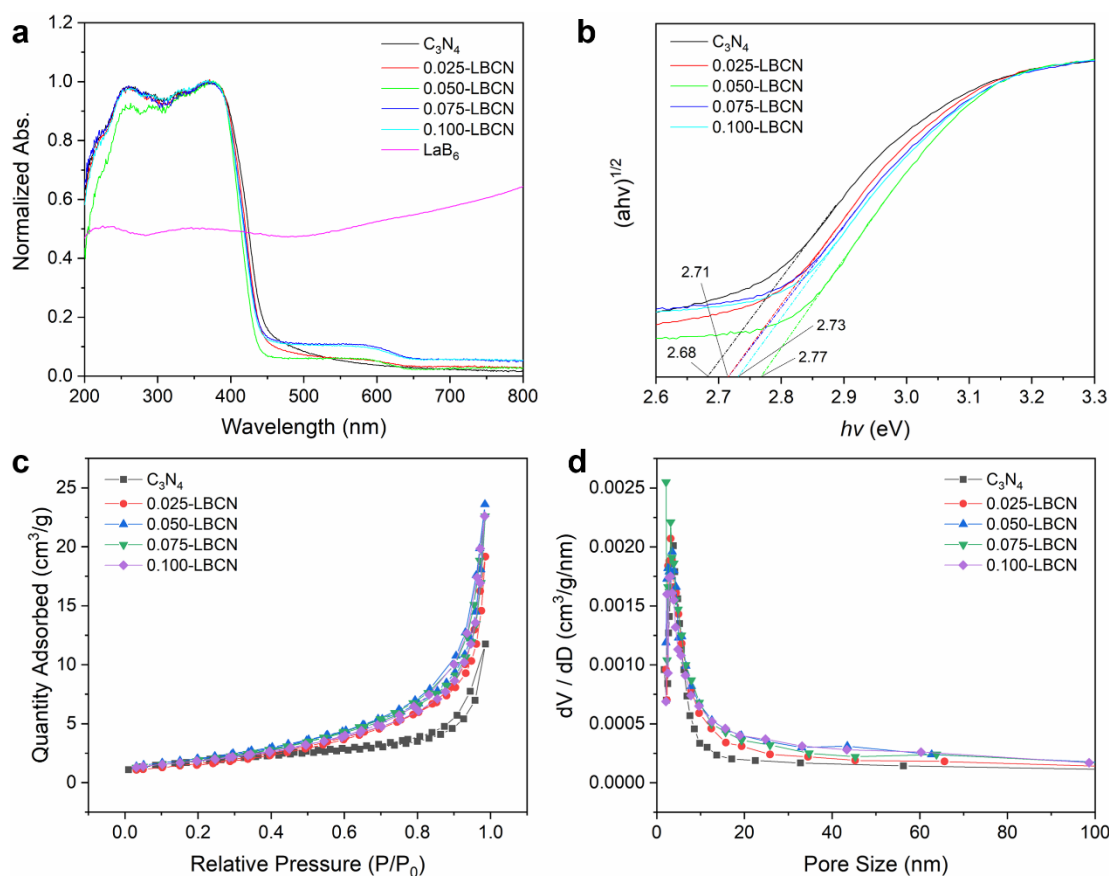


Figure 4. (a) UV-Vis absorption spectra; (b) Tauc plots of the as-obtained samples; (c) N_2 adsorption-desorption isotherms; (d) the corresponding pore size distribution curves of the as-obtained samples.

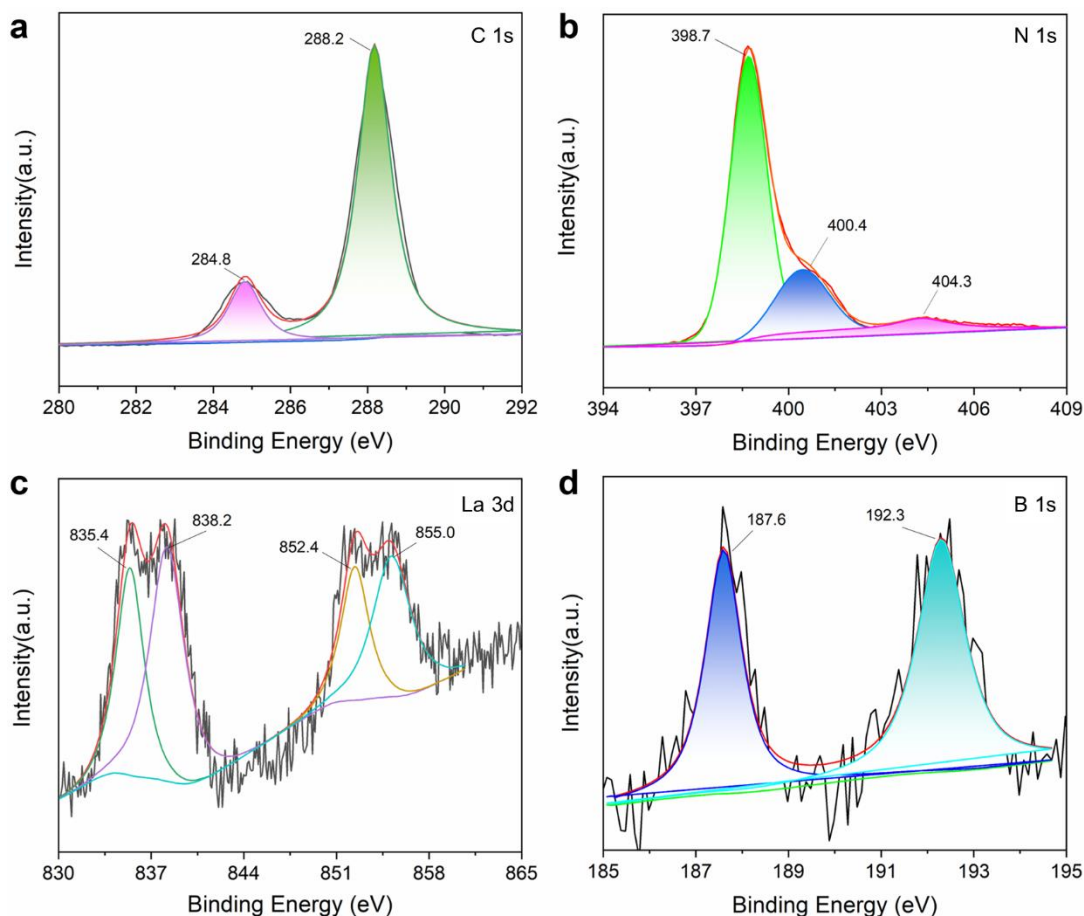


Figure 5. High-resolution XPS spectra of the 0.075-LBCN sample: (a) C 1s; (b) N 1s; (c) La 3d; (d) B 1s.

3.1.4. Chemical Composition and Valence State of the Elements in the Photocatalysts

We also characterized the as-obtained samples' chemical compositions and valence states by using XPS. The high-resolution XPS spectra of C 1s, N 1s, La 3d, and B 1s are displayed in Figures 5a ~ d, respectively. As shown in Figure 5a, there are two peaks shown in C 1s XPS spectrum, which could be assigned to C-C (284.8 eV) and N-C=N in $g\text{-C}_3\text{N}_4$ (288.2 eV). The N 1s XPS plots are fitted into three peaks (see Figure 5b), located at 398.7, 400.4, 404.3 eV, attributing to C-N=C, C-N-H and C=N-B conjugated structure, respectively. The N-C=N peak at 288.2 eV and C-N=C peak located around 398.7 eV were observed in the co-doped samples, indicating the formation of $g\text{-C}_3\text{N}_4$ (He et al., 2017). In the La 3d XPS spectrum of Figure 5c, peaks at 835.4 and 852.4 eV could be assigned to La 3d_{5/2} and La 3d_{3/2}, respectively, indicating the formation of La³⁺ in La₂O₃, which are connected with O in the $g\text{-C}_3\text{N}_4$ network. In contrast, the other pair of 838.2 and 855.0 eV for La 3d_{5/2} and La 3d_{3/2} could be attributed to La in LaB₆. Two peaks are fitted in the B 1s XPS spectrum and are shown in Figure 5d. The peak at 187.6 eV was the typical peak of La-B, while 192.3 eV was the typical peak of N-B (N from the $g\text{-C}_3\text{N}_4$ network). Combined with La 3d and B 1s spectra of co-doped samples, it proved that the La-B co-doping into the $g\text{-C}_3\text{N}_4$.

3.2. Photocatalytic Activity Analysis

3.2.1. Photocatalytic H₂ Production

The photocatalytic hydrogen generation performance was assessed by using a Xe lamp in a 57.5 mL Pyrex reactor, and 4 mL methanol was used as the sacrificial agent for H₂ production. The photocatalytic H₂ production performances are presented in Figure 6. Figure 6a shows the effect of LaB₆ addition in x-LBCN samples, the LaB₆ treated at 500 °C for 2 h has an intrinsic H₂ production rate. The as-obtained x-LBCN samples exhibited better H₂ production performance under visible light irradiation without noble metals, and pure $g\text{-C}_3\text{N}_4$ showed lower activity than that of the co-doped sample (even though there is some non-active LaB₆ in the co-doped samples). The photocatalytic H₂ production improved with the LaB₆ loading and the optimal co-doped sample was 0.075-LBCN. The total H₂ production in 4 h for 0.075-LBCN was 135.5 μmol. As presented above, the La-B co-doping changed the surface, nanostructure and electronic structures and brought impurity states, active site and charge redistribution, enabling the La-B co-doped $g\text{-C}_3\text{N}_4$ to enhance the charge separation efficiency and H₂ production. The remaining LaB₆ also can be beneficial for the charge transfer and separation. It also should be noted that the 0.100-LBCN with 0.10 g LaB₆ added during the preparation process showed a decreased photocatalytic performance of H₂ production com-

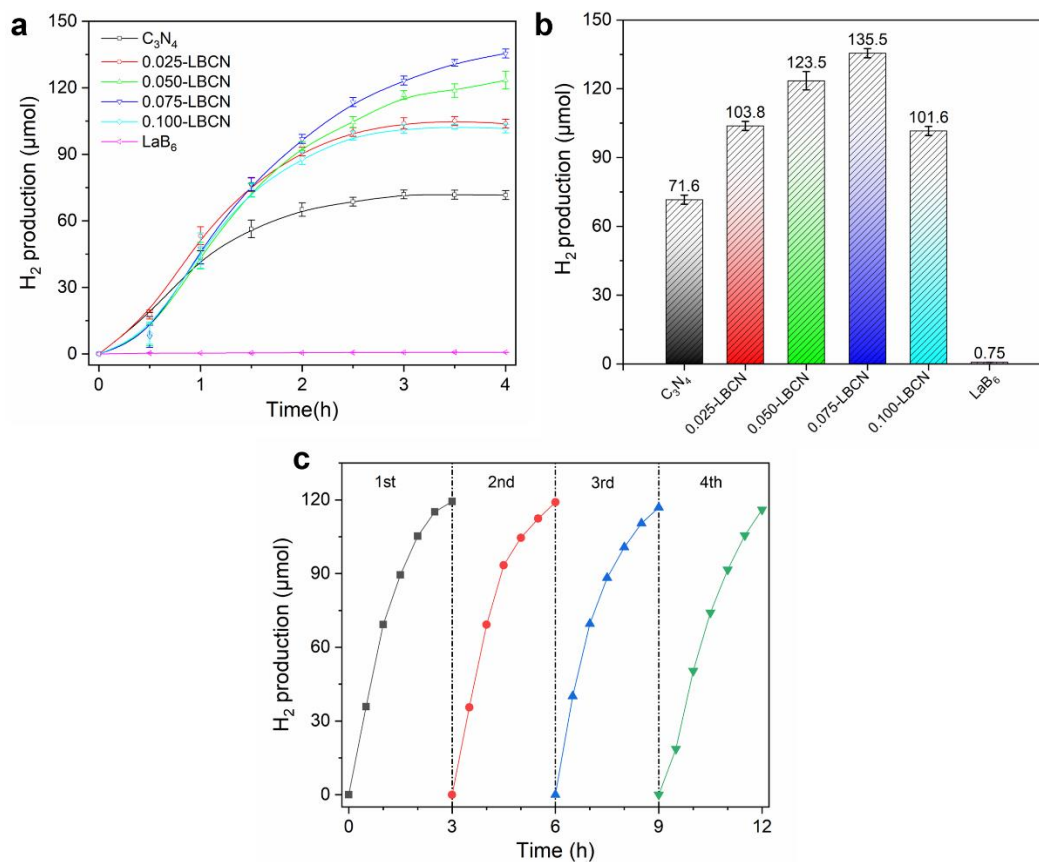


Figure 6. (a) Time profiles of photocatalytic H₂ production in the presence of various La-B co-doped g-C₃N₄ samples; (b) H₂ production amount in the presence of 20 mg various La-B co-doped g-C₃N₄ samples in 4 hours; (c) repeated cycles of H₂ production of the 0.075-LBCN sample, the photocatalyst suspension was evacuated to remove the dissolved gases at the end of each cycle and pump Argon gas at the beginning of the next cycle.

pared to 0.075-LBCN, which could be assigned to the high proportion of non-active LaB₆ and lower active components for photocatalytic H₂ production in the catalyst. The photocatalytic cycle of the optimal sample was also repeated four times (3 h for each cycle) in the same sealed Pyrex reactor in the presence of the same photocatalysts to determine the stability of photocatalytic hydrogen production (Figure 6c). The total H₂ production in 3 h for 0.075-LBCN at the first cycle was 119.24 μmol and reduced to 116.07 μmol after the fourth cycle (about 2.66% decrease), indicating co-doped g-C₃N₄ process stable photocatalytic H₂ production.

3.2.2. Photocatalytic Degradation of RhB

Another visible-light-driven photocatalytic performance is evaluated by degradation of RhB to investigate the photo-redox capability. As shown in Figure 7, the 0.025-LBCN shows the best photocatalytic degradation performance. The removal efficiency of RhB could reach nearly 95% after 120 mins, while the pure LaB₆ shows little removal efficiency for RhB (around 10%). It should be noted that the La-B co-doped samples show better photocatalytic degradation performances compared with the pure g-C₃N₄ and LaB₆. Furthermore, the RhB degradation rate constant of all samples can be calculated using the degrada-

tion data and their values are listed in Table 1. The highest degradation rate constant (k) of the La-B co-doped g-C₃N₄ is up to 0.02315 min⁻¹, 2 times the fold of pure g-C₃N₄ (0.01096 min⁻¹). Other values of the degradation rate constant (k) can be seen in Table 1. Radical trapping experiments are performed to identify the contribution of reactive species, which is better for understanding the electron transfer mechanism. In the radical trapping experiment, ethylenediaminetetraacetic acid disodium salt (EDTA-2Na), benzoquinone (BQ), silver nitrate (AgNO₃), and isopropanol (IPA) were used as effective scavengers for photogenerated holes (h⁺), photogenerated superoxide radical (·O²⁻), photogenerated electrons (e⁻), and hydroxyl radical (·OH), respectively. As shown in Figure 8, the removal efficiencies of RhB in the presence of 1.0-TBCN were decreased to 69.1, 54.8, 90.5, and 48.7% with the addition of EDTA-2Na, BQ, AgNO₃, and IPA under light irradiation for 120 mins, respectively. IPA, BQ, and EDTA-2Na were greatly influenced the removal efficiency of RhB, demonstrating that ·OH, ·O²⁻ and h⁺ played crucial roles in the photodegradation of RhB in our system. It also should be noted that the photocatalytic oxidation ability is essential for the photodegradation of RhB. Combined with the H₂ production data, La-B co-doping could increase the photocatalytic reduction and oxidation ability.

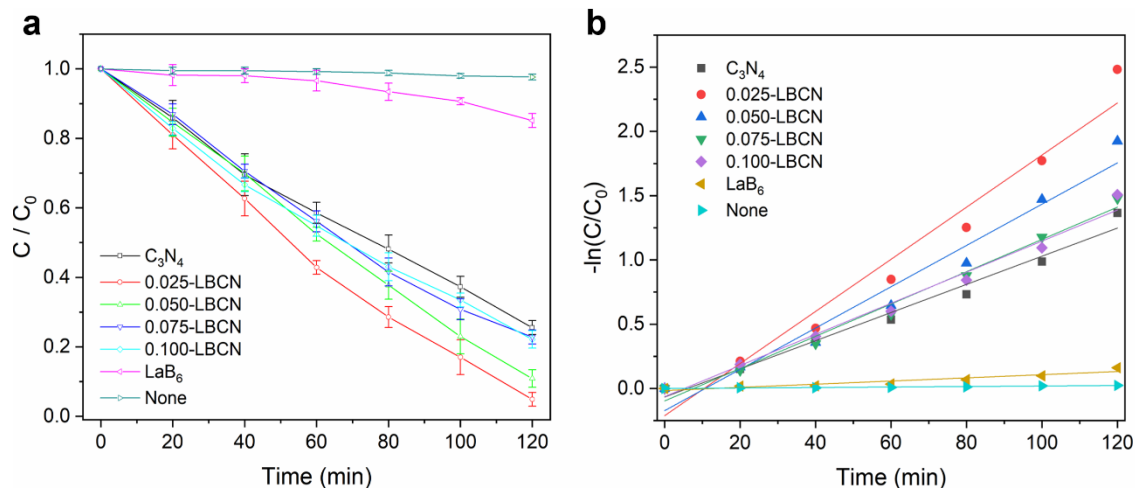


Figure 7. Photocatalytic degradation performances of the as-synthesized samples: (a) the variation of RhB concentration with irradiation time; (b) the corresponding First-order kinetic fitting curves.

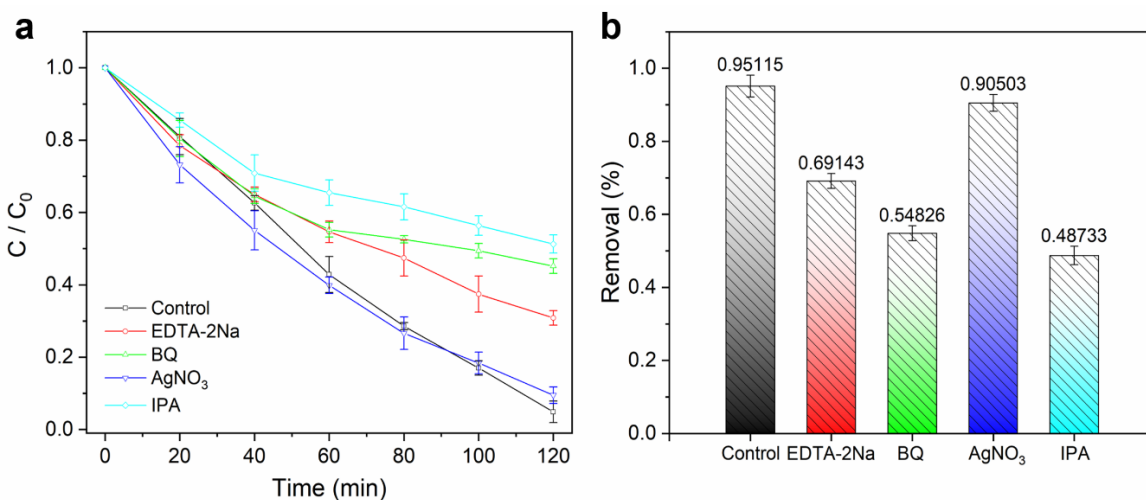


Figure 8. (a) Temporal courses of photocatalytic degradation in the presence of various scavengers; (b) comparison of the degradation rate of RhB in the presence of various scavengers.

3.2.3. Band Position of the La-B Co-Doped $g-C_3N_4$

To investigate the electronic structures of La-B co-doped $g-C_3N_4$, it is required to determine the band energy levels of each sample. As we all know, the redox capability and efficiency of charge transmission and separation are affected by the positions of the conduction band (CB) and valence band (VB) of photocatalysts. Herein, the potential positions of VB were examined by the valence band XPS spectroscopy (VB-XPS) and present in Figure 9a. The values of EVB about $g-C_3N_4$ and La-B co-doped $g-C_3N_4$ were about 1.67, 1.75, 1.71, 1.76 and 1.50 eV, respectively. The values of the bandgap were calculated before, so the values of ECB were calculated. A schematic illustration of the band structures of all samples was drawn according to these calculated potentials of CB and VB edges, as presented in Figure 9b. The CB and VB potentials of 0.025-LBCN were more negative than other samples, which enhanced the effective transmission and separation of photogenerated charges.

Therefore, RhB could be degraded more efficiently than other samples. By the way, the appropriate doping amount was beneficial for photocatalytic reduction for H_2 production. As shown in Figure 9c, we draw the proposed structure of La-B co-doped $g-C_3N_4$ based on our data. It could be seen that the La atoms formed chemical bonds with O or N into the tri-s-triazine units in $g-C_3N_4$. B atoms often interacted with the N in the $g-C_3N_4$ network, which could form chemical bonds with N or replaced the C in the $g-C_3N_4$ network. Appropriate La-B co-doping will result in the formation of the defect and its energy level, high light absorption, nanostructures and electronic structures. The La and B doping also introduces some defect sites, which can trap the photogenerated electron and holes. The efficient charge separation resulting from La-B co-doped will improve the photocatalytic activities (H_2 production and photodegradation of RhB). It also should be noted that few LaB_6 in the catalysts can act as co-catalysts for charge transmission and separation.

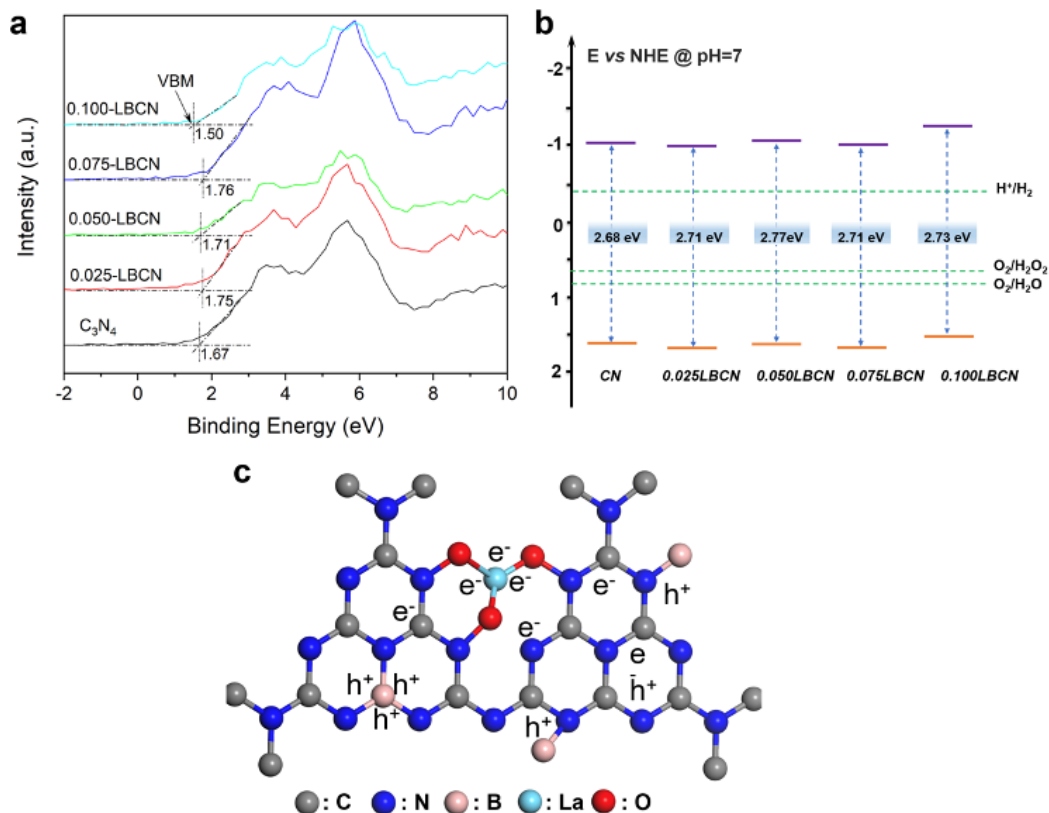


Figure 9. (a) Valence band (VB) XPS spectra; (b) proposed band structure for the various La-B co-doped g-C₃N₄; (c) proposed structure of La-B co-doped g-C₃N₄.

4. Conclusions

In summary, we built the La-B co-doped g-C₃N₄ by an in-situ growth of g-C₃N₄ on LaB₆. This doping has changed the morphologies and electronic structures compared with pure g-C₃N₄, which provide better light-harvesting and reduced charge recombination. The photocatalytic measurements show that the co-doped samples process a higher photocatalytic performance in H₂ production and organic pollution degradation in comparison to the pure g-C₃N₄. The La-B co-doping could change the surface, nanostructure and electronic structure, resulting in impurity states, active sites, charge redistribution and separation. Furthermore, the few LaB₆ in the catalysts could act as a co-catalyst for the charge separation. Our research provides a strategy for the future one-step in-situ growth of efficient co-doped photocatalysts using metal borides.

Acknowledgements. This project was supported by grants from the Fundamental Research Funds for the Central Universities, South Central Minzu University (Nos. CZY20031 and KTZ20043).

References

Anaraki, M.V., Mahmoudian, F., Chianeh, F.N. and Farzin, S. (2022). Dye pollutant removal from synthetic wastewater: A new modeling and predicting approach based on experimental data analysis, kriging interpolation method, and computational intelligence techniques.

- J. Environ. Inform.*, <https://doi.org/10.3808/jei.202200473>
- Bhagat, B.R. and Dashora, A. (2021). Understanding the synergistic effect of Co-loading and B-doping in g-C₃N₄ for enhanced photocatalytic activity for overall solar water splitting. *Carbon*, 178(10), 666-677. <https://doi.org/10.1016/j.carbon.2021.03.049>
- Bouzidi, A., Hussien, M.S.A., Abd-Rabboh, H.S.M., Abdelrhim, A.A. H., Yahia, I.S. and Awwad, N.S. (2020). Physicochemical characterization of La-doped g-C₃N₄ for degradation of phenol and organic dye. *Desalination Water Treat.*, 204, 136-143. <https://doi.org/10.5004/dwt.-2020.26247>
- Cao, G.X., Li, Y.G., Zhang, Q.H. and Wang, H.Z. (2010). Hierarchical porous, self-supporting La- and F-codoped TiO₂ with high durability for continuous-flow visible light photocatalysis. *J. Am. Ceram. Soc.*, 93(5), 1252-1255. <https://doi.org/10.1111/j.1551-2916.2009.03552.x>
- Chang, S.Y. and Kashani, F.R. (2009). Linear programming method for investigating the disposal histories and locations of pollutant sources in an aquifer. *J. Environ. Inform.*, 13(1), 1-11. <https://doi.org/10.3808/jei.2009001-36>
- Chen, P., Wang, H., Liu, H.J., Ni, Z.L., Li, J.Y., Zhou, Y. and Dong, F. (2019). Directional electron delivery and enhanced reactants activation enable efficient photocatalytic air purification on amorphous carbon nitride co-functionalized with O/La. *Appl. Catal. B*, 242, 19-30. <https://doi.org/10.1016/j.apcatb.2018.09.078>
- Cheng, L., Zhang, H.W., Li, Fan, J.J. and Xiang, Q.J. (2021). Carbon-graphitic carbon nitride hybrids for heterogeneous photocatalysis. *Small*, 17(1), 2005231. <https://doi.org/10.1002/smll.202005231>
- Dai, M., He, Z.L., Zhang, P., Li, X. and Wang S.G. (2022). ZnWO₄-ZnIn₂S₄ S-scheme heterojunction for enhanced photocatalytic H₂ evolution. *J. Mater. Sci. Technol.*, 122, 231-242. <https://doi.org/1->

- 0.1016/j.jmst.2022.02.014
- Dhanushkodi, S.R., Mahinpey, N., Srinivasan, A. and Wilson, M. (2015). Life cycle analysis of fuel cell technology. *J. Environ. Inform.*, 109(1), 36-44. <https://doi.org/10.3808/jei.200800109>
- Feng, Y.B., Du, Y., Du, M.X., Li, Z.F., He, Z.L., Yang, K., Lv, X.G., Jiang, N and Liu, Y. (2018). Facile constructing novel 3D porous g-C₃N₄/BiOBr_{0.2}I_{0.8} hybrids: Efficient charge separation for visible-light photocatalysis. *J. Alloys Compd.*, 767, 241-252. <https://doi.org/10.1016/j.jallcom.2018.07.098>
- Fu, J.W., Yu, J.G., Jiang, C.J. and Bei, C. (2018). g-C₃N₄-based heterostructured photocatalysts. *Adv. Energy Mater.*, 8(3), 1701503. <https://doi.org/10.1002/aenm.201701503>
- Guo, P.Y., Zhao, F.Y. and Hu, X.M. (2021). Fabrication of a direct Z-scheme heterojunction between MoS₂ and B/Eu-g-C₃N₄ for an enhanced photocatalytic performance toward tetracycline degradation. *J. Alloys Compd.*, 867, 159044. <https://doi.org/10.1016/j.jallcom.2021.159044>
- He, Z.L., Kim, C.H., Jeon, T.H. and Choi, W.Y. (2018). Hydrogenated heterojunction of boron nitride and titania enables the photocatalytic generation of H₂ in the absence of noble metal catalysts. *Appl. Catal. B*, 237, 772-782. <https://doi.org/10.1016/j.apcatb.2018.06.008>
- He, Z.L., Kim, C.H., Lin L.H., Jeon, T.H., Lin, S., Wang, X.C. and Choi, W.Y. (2017). Formation of heterostructures via direct growth CN on h-BN porous nanosheets for metal-free photocatalysis. *Nano Energy*, 42, 58-68. <https://doi.org/10.1016/j.nanoen.2017.10.043>
- He, Z.L., Zhang J, Li X, Guan, S.G., Dai, M.C. and Wang S.G. (2020). 1D/2D heterostructured photocatalysts: From design and unique properties to their environmental applications. *Small*, 16(46), 2005051. <https://doi.org/10.1002/smll.202005051>
- Jiang, W.L., Ruan, Q.S., Xie, J.J., Zhu, Y.F. and Tang, J.W. (2018). Oxygen-doped carbon nitride aerogel: A self-supported photocatalyst for solar-to-chemical energy conversion. *Appl. Catal. B*, 236, 428-435. <https://doi.org/10.1016/j.apcatb.2018.05.050>
- Lan, Z.A., Fang, Y.X., Zhang, Y.F. and Wang, X.C. (2017). Photocatalytic oxygen evolution from functional triazine-based polymers with tunable band structures. *Angew Chem. Int. Ed.*, 130(2), 479-483. <https://doi.org/10.1002/anie.201711155>
- Li, N.X., Li, X.H., Pan, R., Cheng, M., Guan, J., Zhou, J.C., Liu, M.C., Tang, J.W. and Jing, D.W. (2021a). Efficient photocatalytic CO₂ reformation of methane on Ru/La-g-C₃N₄ by promoting charge transfer and CO₂ activation. *Chem. Photo. Chem.*, 5(8), 748-757. <https://doi.org/10.1002/cptc.202100020>
- Li, X., Chang, J.C., Zhang, S.J., Xiao, L.H., Wu, X.G. and He, Z.L. (2021b). Microcystis@TiO₂ nanoparticles for photocatalytic reduction reactions: Nitrogen fixation and hydrogen evolution. *Catalysts*, 11(12), 1443. <https://doi.org/10.3390/catal11121443>
- Li, X., Zhang, J., Zhang, S.J., Xu, S.S., Wu, X.G., Chang, J.C. and He, Z.L. (2021c). Hexagonal boron nitride composite photocatalysts for hydrogen production. *J. Alloys Compd.*, 864, 158153. <https://doi.org/10.1016/j.jallcom.2020.158153>
- Lin, C., Ma, R.H., Wu, Z.P., Xiong, J.F. and Min, M. (2018). Detection of the sensitive inflowing river indicators related to nonpoint source organic pollution: A case study of Taihu Lake. *J. Environ. Inform.*, 32(2), 98-111. <https://doi.org/10.3808/jei.201600343>
- Liu, J.W., Han, R., Wang, H.T., Zhao, Y., Chu, Z. and Wu, H.Y. (2011). Photoassisted degradation of pentachlorophenol in a simulated soil washing system containing nonionic surfactant Triton X-100 with La-B co-doped TiO₂ under visible and solar light irradiation. *Appl. Catal. B*, 103(3-4), 470-478. <https://doi.org/10.1016/j.apcatb.2011.02.013>
- Liu, R.Z., Zhang, K., Zhang, Z.J. and Borthwick, A.G.L. (2016). Watershed-scale environmental risk assessment of accidental water pollution: The case of Laoguan River, China. *J. Environ. Inform.*, 31(2), 87-96. <https://doi.org/10.3808/jei.201600346>
- Liu, S.M., Bi, T.S., Xue, A.C. and Liu, J.Z. (2018). Equivalent model for calculating fault current from inverter-interfaced renewable energy generators. *J. Environ. Inform.*, 32(1), 36-44. <https://doi.org/10.3808/jei.201800392>
- Mavengere, S. and Kim, J.S. (2020). Photocatalytic properties of g-C₃N₄-supported on the SrAl₂O₄:Eu, Dy/SiO₂. *Coatings*, 10(10), 917. <https://doi.org/10.3390/coatings10100917>
- Miao, L.Z., Wang, C., Hou, J., Wang, P.F., Qian, J. and Dai, S.S. (2014). Kinetics and equilibrium biosorption of nano-ZnO particles on periphytic biofilm under different environmental conditions. *J. Environ. Inform.*, 2(23), 1-9. <https://doi.org/10.3808/jei.201400267>
- Muhammad, A., Tahir, M., Al-Shahrani, S.S., AliaSami, A.M. and Rther., S.U. (2020). Template-free synthesis of graphitic carbon nitride nanotubes mediated by lanthanum (La/g-CNT) for selective photocatalytic CO₂ reduction via dry reforming of methane (DRM) to fuels. *Appl. Surf. Sci.*, 504, 144177. <https://doi.org/10.1016/j.apsusc.2019.144177>
- Ngullie, R.C., Alaswad, S.O., Bhuvanewari, K., Shanmugam, P. and Arunachalam, P. (2020). Synthesis and characterization of efficient ZnO/g-C₃N₄ nanocomposites photocatalyst for photocatalytic degradation of methylene blue. *Coatings*, 10(5), 500. <https://doi.org/10.3390/coatings10050500>
- Ong, W.J., Tan, L.L., Ng, Y.H., Yong, S.T. and Chai, S.P. (2016). Graphitic carbon nitride (g-C₃N₄)-based photocatalysts for artificial photosynthesis and environmental remediation: Are we a step closer to achieving sustainability? *Chem. Rev.*, 116(12), 7159-7329. <https://doi.org/10.1021/acs.chemrev.6b00075>
- Ou, H.H., Lin, L.H., Zheng, Y., Yang, P.J., Fang, Y.X. and Wang, X.C. (2017). Tri-s-triazine-based crystalline carbon nitride nanosheet for an improved hydrogen evolution. *Adv. Mater.*, 29(22), 1700008. <https://doi.org/10.1002/adma.201700008>
- Qu, K.A., Chen, W., Guo, J. and He, Z. (2022). A mini-review on preparation of functional composite fibers and their based devices. *Coatings*, 12(4), 473. <https://doi.org/10.3390/coatings12040473>
- Ren, D.D., Shen, R.C., Jiang, Z.M., Lu, X.Y. and Li, X. (2020). Highly efficient visible-light photocatalytic H₂ evolution over 2D-2D CdS/Cu₂S₄ layered heterojunctions. *Chinese J. Catal.*, 41(1), 31-40. [https://doi.org/10.1016/S1872-2067\(19\)63467-4](https://doi.org/10.1016/S1872-2067(19)63467-4)
- Rong, X.S., Qiu, F.G., Rong, J., Yan, J., Zhao, H., Zhu, X.L. and Yang, D.Y. (2015). Synthesis of porous g-C₃N₄/La and enhanced photocatalytic activity for the degradation of phenol under visible light irradiation. *J. Solid State Chem.*, 230, 126-134. <https://doi.org/10.1016/j.jssc.2015.07.003>
- Shen, R.C., He, K.L., Zhang, A.P., Li, N., Ng, Y.H., Zhang, P., Hu, J. and Li, X. (2021). In-situ construction of metallic Ni₃C@Ni core-shell cocatalysts over g-C₃N₄ nanosheets for shell-thickness-dependent photocatalytic H₂ production. *Appl. Catal. B*, 291, 120104. <https://doi.org/10.1016/j.apcatb.2021.120104>
- Tang, Q.J., Sun, Z.X., Deng, S., Wang, H.Q. and Wu, Z.B. (2020). Decorating g-C₃N₄ with alkalized Ti₃C₂ MXene for promoted photocatalytic CO₂ reduction performance. *J. Colloid. Interface Sci.*, 564, 406-417. <https://doi.org/10.1016/j.jcis.2019.12.091>
- Tasleem, S. and Tahir, M. (2021). Synergistically improved charge separation in bimetallic Co-La modified 3D g-C₃N₄ for enhanced photocatalytic H₂ production under UV-Visible light. *Int. J. Hydrog. Energy*, 46(40), 20995-21012. <https://doi.org/10.1016/j.ijhydene.2021.03.235>
- Thaweesak, S., Wang, S., Lyu, M., Xiao, M., Peerakiathajohn, P. and Wang, L.Z. (2017). Boron-doped graphitic carbon nitride nanosheets for enhanced visible-light photocatalytic water splitting. *Dalton Trans.*, 46(32), 10714-10720. <https://doi.org/10.1039/C7D-T00933J>
- Wang, J.C., Hou, Y.X., Feng, F.D., Wang, W.X., Shi, W.N., Zhang, W.Q., Li, Y., Luo, H.H. and Cui, C.X. (2021a). A recyclable molten-salt synthesis of B and K co-doped g-C₃N₄ for photocatalysis of overall water vapor splitting. *Appl. Surf. Sci.*, 537, 148014. <https://doi.org/10.1016/j.apsusc.2020.148014>
- Wang, M., Che, Y.S., Niu, C., Dang, M.Y. and Dong, D. (2013).

- Lanthanum and boron co-doped BiVO₄ with enhanced visible-light photocatalytic activity for degradation of methyl orange. *J. Rare Earths*, 31(9), 878-884. [https://doi.org/10.1016/S10020721\(1-2\)6037-3-1](https://doi.org/10.1016/S10020721(1-2)6037-3-1)
- Wang, Q., Lin, Y.M., Li, P.Y., Ma, M.T., Maheskumar, V., Jiang, Z.Y. and Zhang, R.Q. (2021b). An efficient Z-scheme (Cr, B) co-doped g-C₃N₄/BiVO₄ photocatalyst for water splitting: a hybrid DFT study. *Int. J. Hydrog. Energy*, 46(1), 247-261. <https://doi.org/10.1016/j.ijhydene.2020.09.252>
- Wang, Y.L., Tian, Y., Lang, Z.L., Guan, W. and Yan, L.K. (2018a). A highly efficient Z-scheme B-doped g-C₃N₄/SnS₂ photocatalyst for CO₂ reduction reaction: a computational study. *J. Mater. Chem. A*, 6(42), 21056-21063. <https://doi.org/10.1039/C8TA07352J>
- Wang, Z., Chen, M., Huang, Y., Shi, X.J., Zhang, Y.F., Huang, T.T., Cao, J.J., Ho, W.K. and Lee, S.C. (2018b). Self-assembly synthesis of boron-doped graphitic carbon nitride hollow tubes for enhanced photocatalytic NO_x removal under visible light. *Appl. Catal. B*, 239, 352-361. <https://doi.org/10.1016/j.apcatb.2018.08.030>
- Xiao, L.H., Li, X., Zhang, J. and He, Z.L. (2021). MgB₄ MXene-like nanosheets for photocatalytic hydrogen evolution. *ACS Appl. Nano Mater.*, 4(11), 12779-12787. <https://doi.org/10.1021/acsanm.1c03497>
- Xiao, W.H., Wang, J.H., Huang, Y.H., Sun, S.C. and Zhou, Y.Y. (2015). An approach for estimating the nitrobenzene (NB) emission effect in frozen rivers: A case study of nitrobenzene pollution in the Songhua River, China. *J. Environ. Inform.*, 26(2), 140-147. <https://doi.org/10.3808/jei.201500323>
- Yan, Q., Huang, G.F., Li, D.F., Zhang, M., Pan, A.L. and Huang, W.Q. (2018). Facile synthesis and superior photocatalytic and electrocatalytic performances of porous B-doped g-C₃N₄ nanosheets. *J. Mater. Sci. Technol.*, 34(12), 2515-2520. <https://doi.org/10.1016/j.jmst.2017.06.018>
- Yan, S.C., Li, Z.S. and Zou, Z.G. (2010). Photodegradation of Rhodamine B and Methyl Orange over Boron-doped g-C₃N₄ under visible light irradiation. *Langmuir*, 26(6), 3894-3901. <https://doi.org/10.1021/la904023j>
- Yao, X.X., Zhang, W.J., Huang, J.L., Du, Z.W., Hong, X.K., Chen, X.F., Hu, X.L. and Wang X.H. (2020). Enhanced photocatalytic nitrogen fixation of Ag/B-doped g-C₃N₄ nanosheets by one-step in-situ decomposition-thermal polymerization method. *Appl. Catal. A-Gen.*, 601, 117647. <https://doi.org/10.1016/j.apcata.2020.117647>
- Youssef, A.M. and Yakout, S.M. (2020). Superior sunlight photocatalytic of N/La codoped ZnO nanostructures synthesized using different chelating agents. *Opt. Mater.*, 107, 110072. <https://doi.org/10.1016/j.optmat.2020.110072>
- Yu, H.L., Xu, S.S., Zhang, S.J., Wang, S.G. and He, Z.L. (2022). In-situ construction of core-shell structured TiB₂-TiO₂@g-C₃N₄ for efficient photocatalytic degradation. *Appl. Surf. Sci.*, 579, 152201. <https://doi.org/10.1016/j.apsusc.2021.152201>
- Yu, R.F., Chen, H.W., Cheng, W.P. and Huang, H.D. (2017). Applying online image analysis to simultaneously evaluate the removals of suspended solids and color from textile wastewater in chemical flocculated sedimentation. *J. Environ. Inform.*, 29(1), 29-38. <https://doi.org/10.3808/jei.201500303>
- Yu, X., Hu, C.G., Hao, D.N., Liu, G., Xu, R., Zhu, X.D., Yu, X., Ma, G.Q. and Ma, L. (2021). Tubular carbon nitride with hierarchical network: Localized charge carrier generation and reduced charge recombination for high-performance photocatalysis of H₂ and H₂O₂ production. *Solar RRL*, 5(5), 2000827. <https://doi.org/10.1002/solr.202000827>
- Yuan, Y.W., Zhang, L.L., Xing, J., Utama, M.I.B., Lu, X., Du, K.Z., Li, Y.M., Hu, X., Wang, S.J., Genc, A., Dunin-Borkowski, R., Arbiol, J. and Xiong, Q.H. (2015). High-yield synthesis and optical properties of g-C₃N₄. *Nanoscale*, 7(29), 12343-12350. <https://doi.org/10.1039/C5NR02905H>
- Zhang, J., Li, X., Guo, J., Zhou, G.H., Xiang, L., Wang, S.G. and He, Z.L. (2022). Novel TiO₂/TPU composite fiber-based smart textiles for photocatalytic applications. *Mater. Adv.*, 3, 1518-1526. <https://doi.org/10.1039/D1MA01200B>
- Zhang, S.W., Li, J.X., Zeng, M.Y., Li, J., Xu, J.L. and Wang, X.K. (2014). Bandgap engineering and mechanism study of nonmetal and metal ion co-doped carbon nitride: C+Fe as an example. *Chem. Eur. J.*, 20(31), 9805-9812. <https://doi.org/10.1002/chem.201400060>
- Zhang, S.J., He, Z.L., Li, X., Zhang, J., Zang, Q.H. and Wang, S.G. (2020). Building heterogeneous nanostructures for photocatalytic ammonia decomposition. *Nanoscale Adv.*, 2(9), 3610-3623. <https://doi.org/10.1039/D0NA00161A>
- Zhang, S.J., He, Z.L., Xu, S.S., Li, X., Zhang, J., Zhan, X.P., Dai, M.C. and Wang, S.G. (2021). In situ liquid-phase growth strategies of g-C₃N₄ solar-driven heterogeneous catalysts for environmental applications. *Solar RRL*, 5(1), 2100233. <https://doi.org/10.1002/solr.202100233>
- Zhao, G., Hao, S.H., Guo, J.H., Xing, Y.P., Zhang, L. and Xu, X.J. (2021). Design of p-n homojunctions in metal-free carbon nitride photocatalyst for overall water splitting. *Chinese J. Catal.*, 42(3), 501-509. [https://doi.org/10.1016/S1872-2067\(20\)63670-1](https://doi.org/10.1016/S1872-2067(20)63670-1)
- Zhu, Z.R., Xia, H.W., Wu, R.N., Cao, Y.Q. and Li., H. (2021). Fabrication of La₂O₃/g-C₃N₄ heterojunction with enhanced photocatalytic performance of tetracycline hydrochloride. *Catalysts*, 11(11), 1349. <https://doi.org/10.3390/cryst11111349>